Design and Assessment of External Insulation for Critical Components in a Medium Voltage SiC-Based Converter via Optical Method

Chongxing Zhang, Yue Xu, *Student Member, IEEE*, Ming Dong, *Member, IEEE*, Rolando Burgos, *Member, IEEE*, Ming Ren, *Member, IEEE*, and Dushan Boroyevich, *Fellow, IEEE*

***Abstract*—Exposed metal or insulator to air interfaces widely exists in medium voltage SiC-based converters. To effectively address external insulation along such interfaces, a large insulation distance in the air is applied. However, such insulation tends to significantly impair converter power densities and performances. Targeting the external discharge free design approaches that reflect the relationship between insulation structures and square wave excitation parameters is highly demanded. Moreover, due to possible fabrication issues and insulation degradation, massive external discharges may still occur, even that they should be eliminated by the design. Therefore, insulation assessment for the entire system, or at least for critical components, is necessary. In this article, silicon photomultiplier (SiPM)-based external discharge detection solutions are introduced. Then, for a self-designed SiC-based medium voltage converter, the SiPM sensors enable both its external insulation design and assessment. By using SiPM sensors, two types of external discharges are characterized under square wave excitation, and thus, general design suggestions are developed. Moreover, as shown by two examples, SiPM sensors can be used to assess the external insulation for converter applications. Based on the experimental data, analysis, and real examples, the results of this study can be used to design and assess the external insulation for future medium voltage, high-power density SiC-based converters.**

***Index Terms*—External insulation design and assessment, medium voltage (MV) silicon carbide (SiC)-based converter, power electronics building block (PEBB), silicon photomultiplier (SiPM)-based sensor.**

I. Introduction

SILICON carbide (SiC)-based medium voltage (MV) power converters can operate at higher power ratings with faster switching speeds and fewer devices than Si-based converters. This advantage stems from higher blocking voltages, faster switching transients, and smaller switching-related losses compared to Si devices. Therefore, SiC-based converters demonstrate an enhanced power density with better efficiency and a more simplified topology than their Si-based counterparts. Researchers are increasingly interested in the use of SiC-based converters for MV high-power applications, such as transportation, industrial motor drives, and ac or dc power distribution [1]–[4].

Because of the high power density requirement and the fast switching transients, a large overdesigned insulation size, which is common practice for Si-based MV converters, cannot accommodate SiC-based converters. Therefore, insulation design, assessment, and online monitoring for individual components, as well as insulation coordination among the components or even among adjacent converters, have become one of the major design aspects for SiC-based converters and need further investigation [5]–[7].

To reach a compact and reliable insulation system without any partial discharge (PD), the electric field (E-field) intensity inside the converters should be well controlled. Usually, if the PD occurs in defects of solid insulation, it is called internal discharge. In contrast, external discharge occurs when PD takes place in the air along exposed metal or insulation interfaces. Accordingly, methods to study external PD are related to external insulation design and assessment. By using the laminated bus as an example, insulation design and assessment methods to eliminate internal discharges have been discussed in our previous publication [6]. Therefore, in this study, we only consider external insulation issues.

External insulation design can be important for power converters. If external discharges are initiated, they can not only degrade the nearby insulation but also cause the risk of multiple issues to the converter system. Since the power, driving, sensing, and control circuits are highly coupled inside converters, power converters can be susceptible to external discharges.

We previously developed an MV power electronics building block (PEBB) equipped with 10-kV SiC MOSFET power modules (see Figs. 1 and 2) [4], [8]. Within this PEBB prototype, external discharges can occur at multiple locations resulting in various system hazards (see Fig. 2).

Based on the discharge location and the corresponding hazard to the converter system, all possible external discharge events

Manuscript received August 9, 2019; revised December 2, 2019 and March 4, 2020; accepted May 12, 2020. Date of publication May 20, 2020; date of current version July 31, 2020. This work was supported in part by the U.S. Office of Naval Research under Grant N00014-16-1-2956 and was approved for public release under DCN #43-5588-19. Recommended for publication by Associate Editor J. Wang. *(Corresponding authors: Ming Ren; Yue Xu.)*

Chongxing Zhang, Ming Dong, and Ming Ren are with the State Key Laboratory of Electrical Insulation & Power Equipment, Xi'an Jiaotong University, Xi'an 710049, China (e-mail: zhangcx.123@stu.xjtu.edu.cn; dongming@xjtu.edu.cn; renming@xjtu.edu.cn).

Yue Xu, Rolando Burgos, and Dushan Boroyevich are with the Center for Power Electronics Systems, Bradley Department of Electrical and Computer Engineering, Virginia Polytechnic Institute and State University, Blacksburg, VA 24061 USA (e-mail: yxu72@vt.edu; rolando@vt.edu; dushan@vt.edu).

Color versions of one or more of the figures in this article are available online at https://ieeexplore.ieee.org.

Digital Object Identifier 10.1109/TPEL.2020.2996262

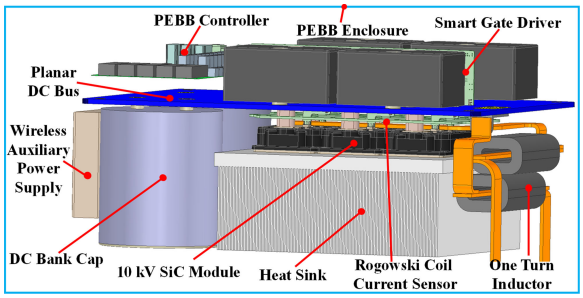

Fig. 1. Three-dimensional drawing of MV PEBB converter prototype.

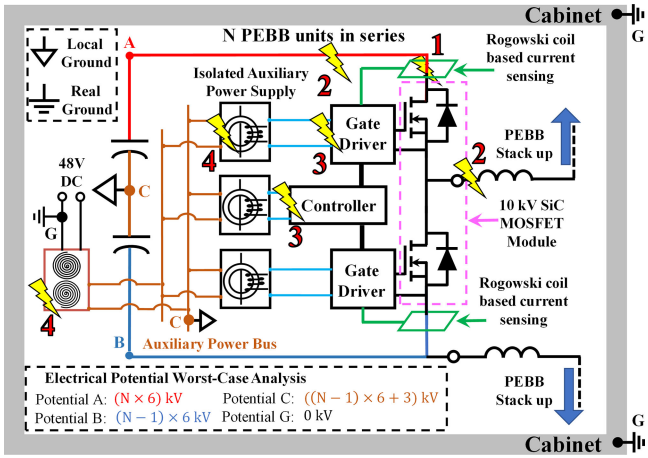

Fig. 2. Schematic of 10-kV SiC MOSFET-based half-bridge converter system. Possible external discharge locations are marked by lightning symbols.

inside the PEBB converter prototype can be divided into four categories.

Type 1: External discharges occurring on sensing circuits can lead to incorrect measurement results that can trigger incorrect operation or protection. These hazards can include discharges between the metal interconnector and the Rogowski coil around it, as discussed in [9].

Type 2: External discharges occurring on the power stage can lead to inrush current through the gate or power terminals of the power module, thereby destroying the modules. As an example of eliminating external discharges on the power stage, we will analyze the external insulation design and assessment for the one-turn inductor used in this PEBB.

Type 3: External discharges occurring on the printed circuit board (PCB) of driving and control circuits can directly damage the integrated circuit (IC) chips and lead to catastrophic failures.

Type 4: External discharges can occur in the isolated auxiliary power supply system, such as between the primary and secondary windings of the transformer. While the transformer itself may not be immediately broken, the auxiliary power bus voltage may collapse owing to such discharges. Moreover, IC chips on the regulation circuit can be destroyed. Therefore, external discharges must be eliminated. We will discuss one example of the external insulation design and assessment for this component in Section V.

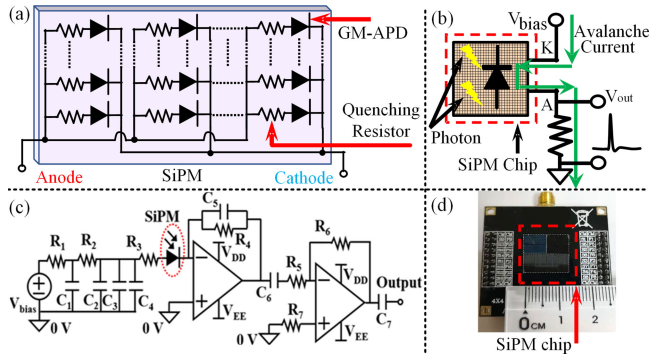

Fig. 3. SiPM-based PD sensor. (a) SiPM equivalent circuit. (b) SiPM working principle. (c) Read-out circuit schematic. (d) SiPM chip with read-out circuit.

The catastrophic failure of converters can be initiated by significant external discharges. Therefore, successful converter prototypes should be designed to eliminate external discharges and incorporate insulation design rules that are supported by experimental data. Meanwhile, external insulation assessments and acceptance testing of real components must be completed, due to possible fabrication issues.

However, for power converter applications, most components in use are sustained to square wave excitation with varied parameters. Under such a square wave excitation, the traditional high-frequency current transformer (HFCT)-based PD detection method can be ineffective on account of the serious impulse displacement current [10]. This problem can be worse for SiC-based applications due to the fast switching transient in this converter type. Accompanied by light radiation, external discharges can alternatively be detected using optical methods, which are hardly affected by the displacement current. Thus, optical discharge detection methods can be more intuitive and effective for power converter applications.

Compared to research on insulation design, offline assessment, and online monitoring in power transmission and distribution systems [11], [12], research on similar topics for power converters remains scarce, even though converters can be more sensitive to discharges. To partially fill this technical gap, we herein introduce a silicon photomultiplier (SiPM)-based optical detection solution to explore external insulation design and assessment in converters. After discussing the structure, working principle, and performance of the introduced sensor, we apply it to extract experimental data from two representative external discharge models under square wave excitation. The results are used to provide external insulation design suggestions. Then, we present designed external discharge free one-turn inductors and transformers in auxiliary power circuits, which are used in the MV PEBB unit (see Fig. 1).

II. Structure, Working Principle, and Performance of the SiPM-Based Optical Sensor

To accurately and effectively detect the external discharge, SiPM based external discharge detection solution is introduced. As shown in Fig. 3, this silicon-based solid-state sensor can capture the photon emission of an external PD with high immunity

to the displacement current and other types of electromagnetic interference (EMI).

An SiPM chip contains a matrix of small-sized sensitive elements [see Fig. 3(a) and (d)]. Each element integrates the photodiode with a quenching resistor and works under the Geiger mode. Thus, the photon radiated by PD can be amplified into a measurable photocurrent and introduce a voltage spike across the quenching resistor [see Fig. 3(b)]. In this study, a commercial SiPM chip (SensL-MicroFJ-30035-TSV) was selected as the photoelectric coupling element with the response spectral range of 200–900 nm. The peak photon detection efficiency of the SiPM chip was approximately 51% at 420 nm under a bias voltage of 25 V. To response photons induced by PD with a high gain, a read-out circuit, including noise suppression, impedance matching, signal amplification, etc., was self-designed [see Fig. 3(c)]. An image of the SiPM chip with its read-out circuit is shown in Fig. 3(d).

The presented SiPM sensor is small (millimeter-level), with the advantages of high gain (up to 10^6 A/W), good sensitivity (approximately 5 to 10 pC), high EMI immunity, and good pulse resolution. Therefore, this SiPM sensor provides a high-performing tool for the design and assessment of external insulation. Moreover, owing to its low power consumption and operation voltage, this sensor can be battery-powered and integrated into converters for online monitoring. Therefore, the SiPM-based detection solution should be more suitable for converter applications than the traditional photomultiplier tube (PMT)-based solutions. More details on the comparison between SiPM and PMT sensors can be found in [13].

III. Experimental Setup for External Discharge Behavior Characterization Under Square Excitation

We captured experimental data from two different external discharge models under square wave excitation with varied parameters via SiPM sensors. After data processing and analyzing, suggestions for external insulation design could be developed and thus further applied to external discharge free, high power density, MV converter design.

A. Two Types of External Discharge Model

External discharge in the air can be divided into two categories. Surface discharge occurs on exposed metal, insulation dielectric, and air interfaces then develop along insulation surfaces. Examples of surface discharge include discharges on exposed metal pads of PCB or metal interconnections of a laminated bus. In contrast, point discharge occurs on exposed metal to air interfaces with no other insulation medium nearby. Point discharge can occur on metal interconnectors among components or adjacent PEBBs.

Both types of external discharges are mainly governed by E-field distribution and influenced by interfacial characterization. Based on this consideration, two typical external discharge models are built, which respectively represent two external discharge categories.

1) rod-plate electrodes with a GPO-3 insulation plate in between [see Fig. 4(a)];

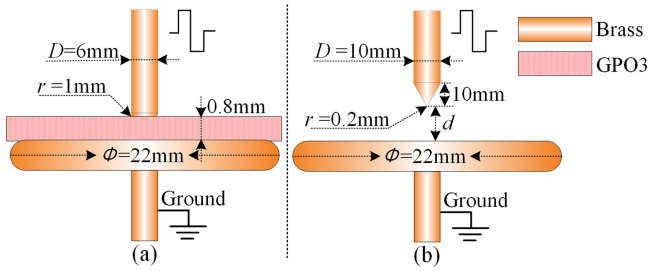

Fig. 4. Test structures for external discharge behavior characterization. (a) Surface discharge (metal-air-insulation interfaces). (b) Point discharge (metal-air interfaces).

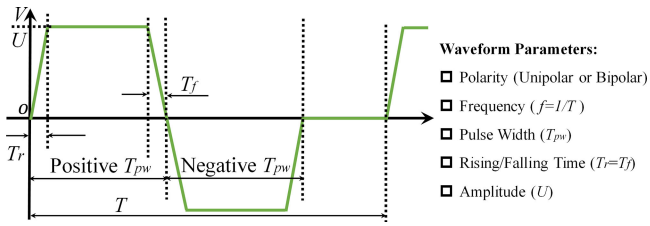

Fig. 5. Parameters of the adjustable square wave excitation.

2) needle-plate electrodes with a certain air gap in between [see Fig. 4(b)].

B. Repetitive Square Excitation and Its Parameters

Square wave excitation includes many parameters that can change during converter operation, depending on the given topologies, modulation methods, and applications. As shown in Fig. 5, these parameters include polarity, rising/falling time, amplitude, duty cycle, and frequency. Since these parameters influence the PD behavior in different ways, the relationship between the external discharge behavior and excitation parameters for two discharge models must be studied to give relatively completed design suggestions for the converter design.

Here, we used a commercial power supply to initiate the square wave excitation with adjustable parameters. For the power supply, the excitation polarity could be either unipolar or bipolar, with the output amplitude up to 25 kV and a continually adjustable rising/falling time in the range of 0.7–70 μs. The pulse width could be tuned from 0 to 150 μs (positive and negative width could be independently tuned) and the excitation frequency could be any point lower than 4 kHz. Simultaneously, an H-bridge circuit with two half-bridge 10-kV SiC MOSFET modules was established to extend the testing range. This H-bridge could generate adjustable square wave excitation with an output magnitude up to 8 kV and a typical rising/falling time of less than 100 ns.

C. External Discharge Experimental Measurement System

The established PD experimental system under square wave excitation is shown in Fig. 6(a). First, the discharge electrodes were fixed and installed by using a self-designed insulating shelf. The entire setup was placed inside a electromagnetic compatibility chamber, which provided a dark environment and

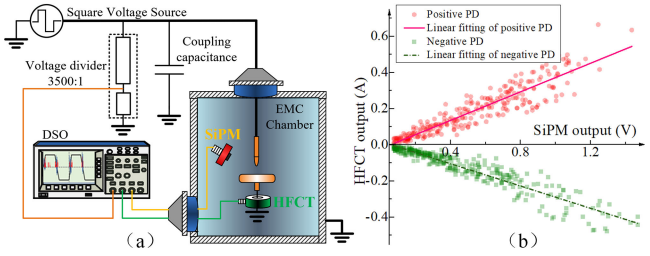

Fig. 6. (a) Synthetic PD measurement system. (b) Linear fitting of optical and electrical PD signals.

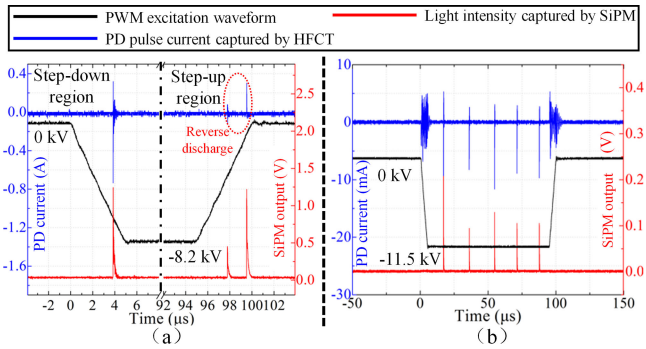

Fig. 7. Typical PD waveform under negative unipolar square excitation for the two external discharge models. (a) Time-domain waveform of surface discharge. (b) Time-domain waveform of point discharge. ($f = 2$ kHz, $T_r = T_f = 5$ μs, $T_{\rm pw} = 100$ μs).

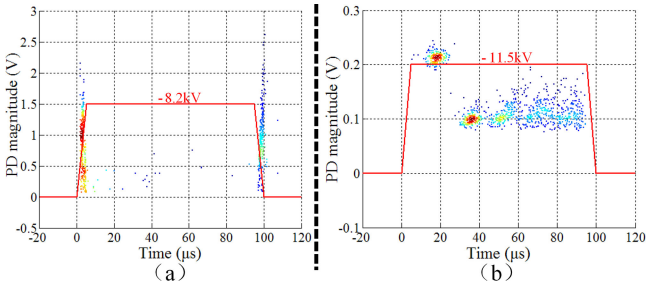

Fig. 8. Typical PRPD patterns under negative unipolar square excitation for the two external discharge models. (a) PRPD pattern of surface discharge. (b) PRPD pattern of point discharge. ($f = 2$ kHz, $T_r = T_f = 5$ μs, $T_{\rm pw} = 100$ μs).

blocked any possible external EMI. Then, the adjustable high-voltage square wave sources were connected to the discharge electrodes. In addition, one HFCT was installed through the grounding wire to capture the PD current pulses. Additionally, a SiPM sensor was placed approximately 20 cm away from the electrodes for optical PD detection. Finally, signals from a voltage divider (3500:1), HFCT, and SiPM sensor were fed to a digital oscilloscope (Tektronix DPO7354).

All tests were conducted at a temperature of 20±1°C, relative humidity of 20%±4%, and normal pressure. According to [14] and [15], such fluctuations of environmental parameters should not significantly affect the discharge behavior. The overall performance of the SiPM sensor was further examined by point discharge under square wave excitation. For the same PD event, the SiPM sensor output and the one from HFCT could be compared. As shown in Fig. 6(b), outputs from the SiPM-based sensor and the HFCT are highly correlated. Both outputs have linear relationships with the discharge level.

IV. Converter External Insulation Design Suggestions Based on External Discharge Characterization

Typical PD waveforms and phase-resolved PD (PRPD) patterns were characterized for the two external discharge models in this section. Then, comprehensive physical mechanisms were depicted to explain the differences in patterns of the two discharge models. Based on the physical mechanism, two kinds of experimental tests were further conducted to develop general external insulation design suggestions for converter applications.

First, we measured the change in PD inception voltage (PDIV) under different polarities, switching speeds, and repetitive frequencies. With increasing the excitation magnitude step by step, when the first PD beyond background noise could be observed and more PD events could also be recognized in the following cycles, the peak value of the applied voltage was recorded as the PDIV(i). For surface discharge, we repeated the experiment ten times (i = 1, 2, …, 10) on the same insulation plate (GPO-3) first. Then we employed a new sample and repeated the entire experiment on a second sample to evaluate the measurement variation between samples. The mean value was regarded as the final PDIV value, which was calculated as

$$\mathrm{PDIV} = \frac{1}{20}\sum_{i=1}^{20}\mathrm{PDIV}(i)(i = 1, 2, \ldots, 20). \tag{1}$$

Second, we examined the influences of the square wave excitation amplitude, frequency, and switching speed on the PD statistical parameters. These PD statistical parameters mainly included the PD average discharge magnitude and PD repetition rate of each excitation cycle, which could be evaluated from the PRPD patterns. Here, we recorded all PD events during 500 excitation cycles. $N_{\rm PD}$ was the total PD number and each PD magnitude was extracted (M_i, $i = 1, 2 \ldots, N_{\rm PD}$) from these cycles. Then, the PD average discharge magnitude ($M_{\rm av}$) was defined as the mean total discharge magnitude of each cycle

$$M_{\rm av} = \frac{1}{500}\sum_{i=1}^{N_{\rm PD}} M_i \,(i = 1, 2, \cdots, N_{\rm PD}). \tag{2}$$

The PD repetition rate ($R_{\rm PD}$) is defined as the mean PD number of each cycle

$$R_{\rm PD} = \frac{N_{\rm PD}}{500}. \tag{3}$$

A. Typical PD Waveforms Under Square Excitation and the General Discharge Mechanism

Typical PD time-domain waveforms for the two external discharge models under negative unipolar square excitation are shown in Fig. 7, and the corresponding PRPD patterns are presented in Fig. 8. The plate electrode was grounded during all experiments.

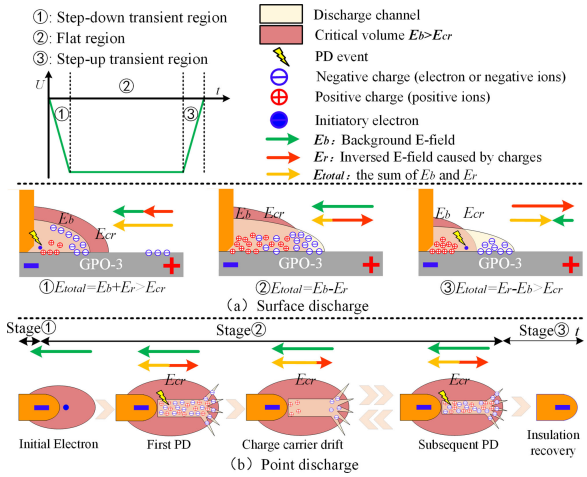

Fig. 9. General physical mechanism for the two discharge models.

A comparison of the experimental results for the two external discharge models (see Figs. 7 and 8) reveals two major differences.

1) Location of the first PD event occurrence for each square wave excitation cycle: For the surface discharge model (metal-air-insulation interfaces), most of the discharge events appear during the switching transient. In contrast, for the point discharge model (metal-air interfaces), the point discharge occurs first in the flat region of the excitation, which is slightly later after the switching transient.

2) Successive discharges after the first discharge event: For the surface discharge model, after the first discharge event in each square wave excitation cycle, there is usually no successive discharge until the next switching transient. In contrast, for the point discharge model, after the first discharge event in each square wave excitation cycle, several successive discharge events occur during the flat region of the excitation.

After a PD event, charges generated by PD can drift toward the electrodes or deposit on the insulator surfaces nearby. These charges are termed space charges or accumulated charges. The two major differences in PD characteristics between the two discharge models can be explained after considering the difference in the charge decay speed. Because of the strong charge accumulation effect on the dielectric surface [16], the decay speed of residual charges along the solid insulator (GPO-3) surface is much slower than that in pure air. Thus, when the first PD event of a square wave excitation cycle is under analysis, the accumulation charge along the GPO-3 surface should be considered. In contrast, the accumulation charge in the air may be neglected depending on the excitation frequency.

According to the three regions in the unipolar square wave excitation shown in Fig. 9, the comprehensive mechanism for the two kinds of external discharges can be described as follows.

a) Step-down transient region of the square wave excitation (Stage ① in Fig. 9): For the surface discharge model, during the excitation step-down transition, in a small volume around the rod tip, the background E-field intensity (E_b) generated by the excitation and the E-field caused by residual charges (E_r) from previous excitation cycles are in the same direction. Thus, the total E-field (E_{total}) can exceed the critical E-field value E_{cr}. The initiatory electrons from accumulated charges can trigger an electron avalanche without a large time lag. Then, because of the fast excitation falling edge, the charge drift velocity is lower than the development speed of the critical E-field boundary, which is beneficial to further discharge propagation. Finally, the avalanche develops into the first PD event with a high discharge magnitude in the excitation cycle under analysis. This PD can be observed for the surface discharge model during the excitation transient in Figs. 7 and 8.

However, under the point discharge model, no charges from previous excitation cycles can turn into effective initiatory electrons for this excitation cycle under analysis on account of the fast space charge decay. Therefore, in a small air volume around the needle electrode tip, although E_b already exceeds E_{cr} during the step-down transient, a certain statistical time lag is necessary to create an initiatory electron. In general, this statistical time lag is longer than the falling time of the excitation. As a result, there are usually no PDs for point discharge during the excitation step-down stage.

b) Flat region of the square wave excitation (Stage ② in Fig. 9): During the excitation flat region, under the surface discharge model, the inverse E-field (E_r) caused by accumulated charges remains at a relatively high magnitude due to the low charge dissipation rate. Moreover, because of the slow charge drift, the inverse E-field (E_r) weakens the background E-field (E_b). Thus, it restrains the occurrence of new discharge. Consequently, there are almost no PDs in this stage.

By comparison, under the point discharge model, the first PD occurs when the initiatory electron is produced. After the first PD, positive and negative ions created by the first PD, drift toward the electrodes. Then, E_r decreases gradually owing to the high charge dissipation rate and E_{total} increases because of the constant background E-field E_b in this stage. When E_{total} recovers to a high level beyond E_{cr}, a successive PD can be triggered. This process can repeat several times within the flat region of the excitation, which results in multiple successive PD events under the point discharge as shown in Figs. 7 and 8.

c) Step-up transient region of the square wave excitation (Stage ③ in Fig. 9): During the excitation step-up transition, the excitation quickly steps up to zero; thus, the background E-field E_b sharply decreases to almost zero. Under the surface discharge model, the reversed E-field E_r can be much greater than E_b owing to the slow dissipation rate of the accumulated charges. Then, E_{total} is the same direction as E_r since it is now dominant. A reversed PD can occur if intensity of E_r is adequately enough.

Under the point discharge model, there are not many positive or negative ions in the space because of the fast charge dissipation velocity in air. Therefore, the E-field introduced by such space charges cannot be high enough to cause an additional PD and a reversed discharge is not observed in this stage.

B. Influence of Excitation Parameters on PDIV Under the Two Discharge Models

It should be noted that there are always some electron avalanches with small discharge levels before the occurrence of the observed streamer-type discharge. However, such small

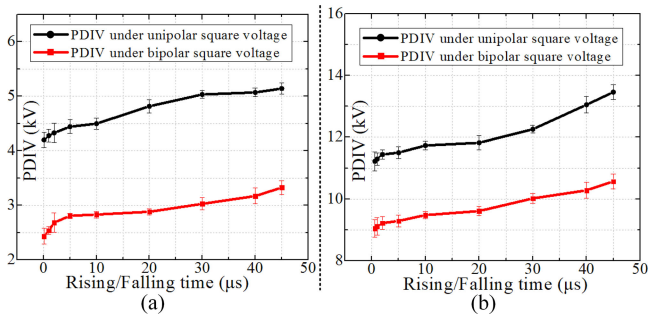

Fig. 10. PDIV depends on the rising/falling time. (a) Surface discharge model ($f = 2$ kHz, $T_{\rm pw} = 100$ μs). (b) Point discharge model ($f = 2$ kHz, $T_{\rm pw} = 100$ μs).

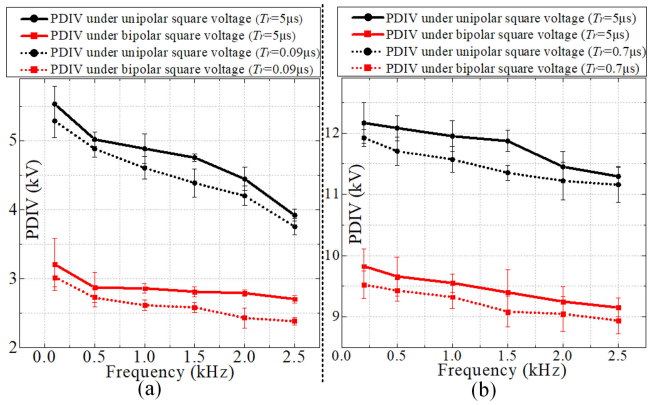

Fig. 11. PDIV depends on the excitation frequency. (a) Surface discharge model ($T_{\rm pw} = 100$ μs) (b) Point discharge model ($T_{\rm pw} = 100$ μs).

avalanches cannot be detected with any of the methods used in this study, even the SiPM sensor. Therefore, a small number of charges could exist in the air near the needle tip or around the triple junction of the rod electrode, before further raising the excitation amplitude to PDIV.

1) Influence of the Excitation Area on PDIV: For both discharge models, because of the polarity effect [17], [18], PDIV under negative unipolar excitation is always lower than that under positive unipolar excitation. Therefore, only negative unipolar excitation is further analyzed.

For negative unipolar excitation, the duration time of high voltage output is fixed at 100 μs. Thus, the integral of background E-field along time, which can be represented by the excitation area, decreases with the increase of the rising/falling time. Since the integral of applied background E-field with time determines the initiatory electron generation probability, the excitation must increase for a higher initiatory electron generation rate, if the entire high-voltage output duration time cannot increase. This results in an increase of PDIV in experiments after the rising/falling time becomes longer. Future work should include a more detailed physical model that matches these experimental data.

2) Influence of Excitation Polarity and dV/dt *on PDIV:* Under the surface discharge model, when the rising/falling time is small (less than approximately 2 μs), in terms of PDIV, the peak-to-peak value of the bipolar excitation is roughly equal to the peak value of the unipolar excitation [see Fig. 10(a)]. This phenomenon was also observed in references [19] and [20] on different surface discharge coupons.

In comparison, under the point discharge model, from the perspective of PDIV, the peak value of bipolar excitation is also lower than that of the unipolar excitation [see Fig. 10(b)]. However, this difference is much smaller than the one observed under the surface discharge model.

Under bipolar excitation, when the background E-field generated by the excitation suddenly changes its direction, the E-field introduced by accumulated charges along the insulation (GPO-3) surface cannot entirely change its direction in the equivalent time frame. This is known as the charge memory effect. Shortly after the excitation reverses its polarity, the total E-field intensity along the insulation (GPO-3) surfaces is the sum of the background E-field and the insulation surface E-field introduced by charges. Therefore, under the high *dV/dt* condition and near insulation (GPO-3) surfaces, where charges cannot quickly deplete, the peak-to-peak value of bipolar excitation should be considered as the driving factor for the PD occurrence. However, such an effect is not that significant for point discharge because of the relatively fast charge decay speed in air.

3) Influence of Excitation Frequency on PDIV: For both the surface and point discharge models, PDIV drops down with the increase of excitation frequency, as shown in Fig. 11. As previously discussed, some small undetectable avalanches occur and, thus, introduce some residual charges in the air or deposited on the GPO-3 surface. These accumulated charges can be more difficult to dissipate at higher excitation frequencies [21] and, thus, enhance the total E-field. Therefore, considering the E-field enhancement by the charges, especially at a high excitation frequency, lower background E-field intensity is required to trigger the streamer discharge. Consequently, a lower PDIV can be observed in Fig. 11 when the frequency increases, at least for the frequency range and test coupons used in this study.

C. Influence of Excitation Parameters on PD Statistical Parameters Under the Two Discharge Models

With the increase of applied voltage amplitude, the background E-field becomes stronger for both discharge models. As a result, the ionization rate in the discharge channel is more intense, which results in higher discharge repetition rate and discharge magnitude, as shown in Fig. 12.

As shown in Fig. 13(a), for the surface discharge model, the average discharge magnitude increases as the excitation frequency increases. Under bipolar excitation, the PD repetition rate drops at a higher frequency; however, it changes only slightly under unipolar excitation. For the point discharge model, as shown in Fig. 13(b), the excitation frequency has almost no influence on both the PD repetition rate and the average discharge magnitude.

Under the surface discharge model, as the rising/falling time increases (*dV/dt* decreases), the PD repetition rate increases under both unipolar and bipolar excitation, whereas the average discharge magnitude decreases significantly, as shown

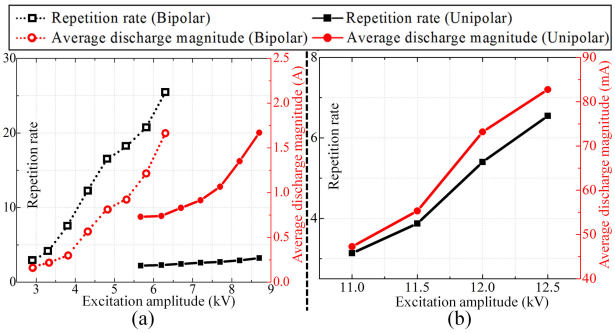

Fig. 12. PD repetition rate and magnitude under different excitation amplitudes. (a) Surface discharge model ($f = 2$ kHz, $T_r = T_f = 5$ μs, $T_{\rm pw} = 100$ μs). (b) Point discharge model ($f = 2$ kHz, $T_r = T_f = 5$ μs, $T_{\rm pw} = 100$ μs).

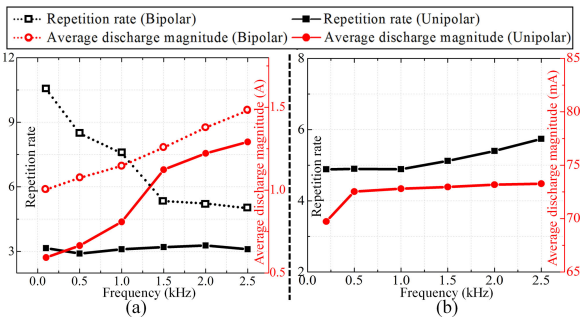

Fig. 13. PD repetition rate and magnitude under different excitation frequencies. (a) Surface discharge model ($T_r = T_f = 5$ μs, $T_{\rm pw} = 100$ μs, $U = 7$ kV for unipolar and 4 kV for bipolar). (b) Point discharge model ($T_r = T_f = 5$ μs, $T_{\rm pw} = 100$ μs, $U = 12$ kV).

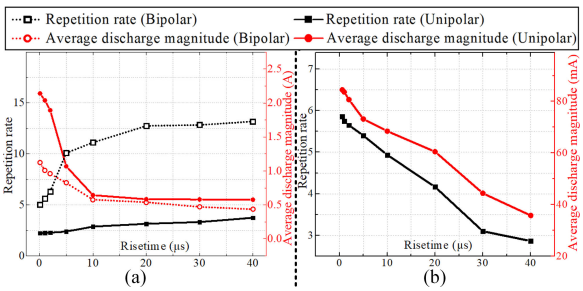

Fig. 14. PD repetition rate and magnitude under different rising/falling times. (a) Surface discharge model ($f = 2$ kHz, $T_{\rm pw} = 100$ μs, $U = 7$ kV for unipolar and 4 kV for bipolar). (b) Point discharge model ($f = 2$ kHz, $T_{\rm pw} = 100$ μs, $U = 12$ kV).

in Fig. 14(a). Under the point discharge model, both the PD repetition rate and average discharge magnitude decrease with an increase in the rising/falling time, as shown in Fig. 14(b).

D. Process of External Insulation Design and Assessment

After combining the experimental data presented here with classical insulation design knowledge, several external insulation designs and assessment suggestions for power electronics application are presented as follows.

1) Owing to the fast switching transient of SiC devices, the peak-to-peak value of bipolar excitation should be used for worst-case background E-field estimation.
2) Based on [22] and the effective ionization coefficient calculation, under the pressure of 760 Torr and regular laboratory conditions, the maximum E-field intensity in the air should be lower than 2.65 kV/mm during external insulation design. Considering the differences in roughness and tolerances of the metal conductors or insulating surfaces and variations in the temperature and humidity of the air, a safety margin of about 20% is applied, then 2 kV/mm is suggested as a design criterion.
3) For E-field management in air, various methods, such as geometrical-based adjustment, high permittivity coating, and guard rings, can be applied to further reduce E-field crowding. Some examples are provided in Section V.
4) If other excitation parameters do not change, the higher the excitation frequency is, the lower the expected PDIV is. This relationship depends on whether the charges can entirely decay during the zero-excitation period between adjacent square-wave cycles. Therefore, for external insulation assessment, excitation parameters that may occur during converter operation should be applied for the test samples.
5) The excitation area within one square wave excitation cycle, which is the integral of excitation amplitude over time, should be considered for PDIV estimation, instead of considering *dV/dt* or pulse width alone.
6) If external discharges are captured during assessment, the PRPD pattern can be used to implement a further insulation diagnosis. The observed discharge patterns should be either close to the surface discharge model or the point discharge model described here. Such information can help discern the insulation weakness points and further improve the external insulation.
7) The PD magnitude and repetition rate can change significantly with the excitation parameters. Such data could help the selection of excitation parameters for both design and assessment aspects. In addition, these data may help the condition selection for fast aging or reliability tests.

The external insulation and assessment should iterate until the final design achieves external discharge free under the normal operating voltage and passes the experimental assessment. To better help with the engineering practice, a flowchart in Fig. 15 can clearly elucidate the iteration process of external insulation design and assessment.

V. Examples of External Insulation Design and Assessment in MV PEBB Converters

The one-turn inductor and the wireless power transferring (WPT) circuit used in the MV PEBB converter can be used as examples of the external insulation design and assessment process.

A. External Insulation Design and Assessment of One-Turn Inductor via SiPM PD Detection Sensor

A one-turn differential mode inductor with a planar coaxial-cable-like structure is integrated into each PEBB unit to limit the circulating current between PEBBs (see Fig. 16). For a 6-kV dc

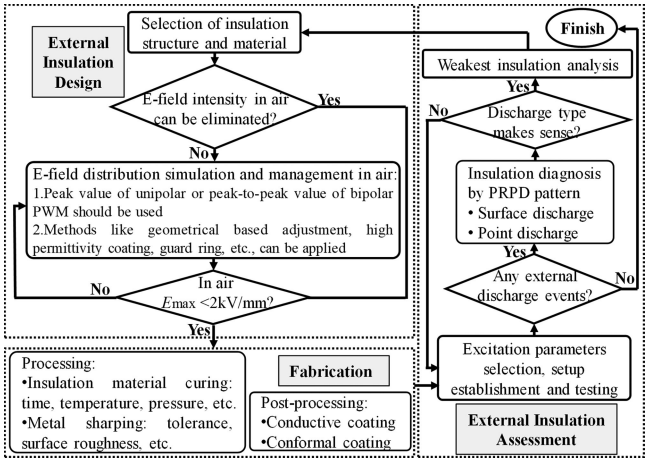

Fig. 15. Proposed iteration process for the design and experimental assessment of external insulation for converters.

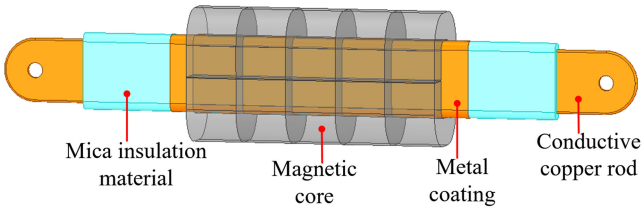

Fig. 16. One-turn inductor with a planar coaxial-cable-like insulation structure.

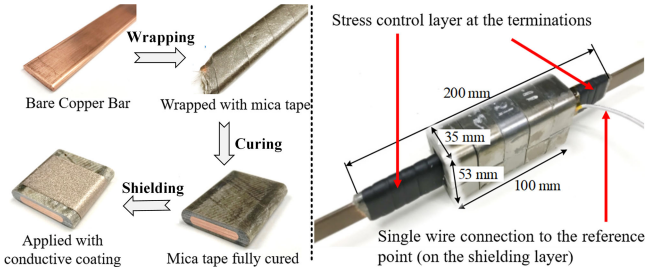

Fig. 17. Fabrication process of the one-turn inductor used in this study.

bus PEBB design, the magnetic cores are shorted to the half dc point, which is 3-kV higher than the negative dc rail in the same cell. A copper bar connects the output terminal of this PEBB with another adjacent PEBB or the load. Since the SiC-based devices have a 10-kV voltage rating, this one-turn inductor should be designed as an external discharge free under bipolar excitation with 5-kV peak value.

A planar coaxial-cable-like structure with reliable insulation is constructed to improve the power density by squeezing the air out of the insulation system. The fabrication process of the one-turn inductor is shown in Fig. 17. The copper bar is first wrapped by Vonroll mica tape (Von Roll 77984 Mica Tape). Then, it is hot-pressed at 160 °C and 120 psi for 1 h. After the tape is fully cured, the conductive coating layer is carefully built on the mica tape surface. This conductive coating layer is finally electrically connected to the reference plane via a single wire connection. Consequently, all electric stress is only applied to

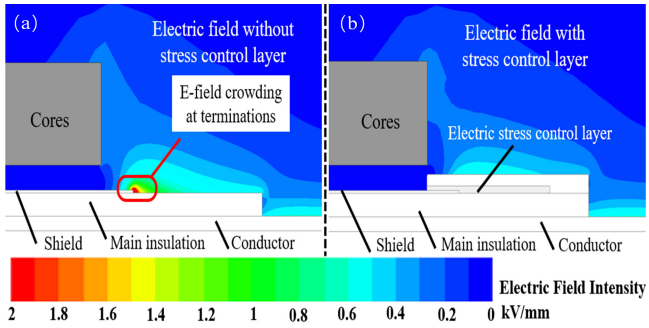

Fig. 18. E-field distribution on the terminations of the proposed one-turn inductor (a) without termination techniques and (b) with termination techniques.

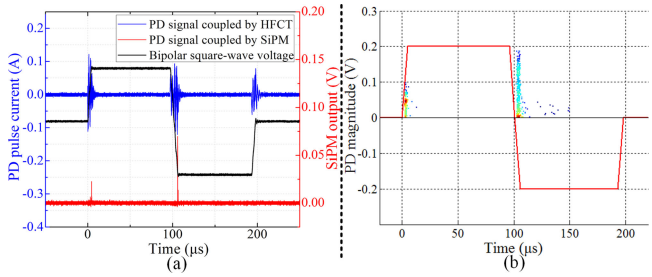

Fig. 19. Experimental results for the coaxial-cable-like one-turn inductor sample (without high-K tape on the terminations) by using the SiPM sensor. (a) PD waveform. (b) PRPD pattern.

the mica layer, instead of being distributed along the air window between the magnetic cores and the copper bar. This technique results in a very compact one-turn inductor design and can be scaled up for higher voltage applications. Moreover, this design informs the inductor optimization, since no extra window area is required for insulation purposes. In addition to the external insulation design and assessment of the inductor shown in this article, more details about the circuit parameters optimization design of this inductor will be separately described in the future.

However, the E-field may crowd at the terminations, which is a common issue with the coaxial cable. Thus, special termination technologies and adequate creepage distance must be applied. For this proposed one-turn inductor design, high permittivity (high-K) tape is selected to relieve the E-field stress at the terminals. Using finite-element analysis (FEA), the E-field distributions around the terminations with and without high-K tape are shown in Fig. 18.

By using the SiPM PD detection sensor, the insulation design at the inductor terminations can be verified. Without any termination techniques, many surface discharges can be observed under bipolar excitation, peaking at approximately 2.5 kV. This observation matches the simulation results, in which approximately 2 kV/mm E-field intensity appears at terminations when 5 kV (peak-to-peak value of bipolar excitation) differential voltage is applied between the copper bar and magnetics. In the experimental results, most of the PD events occur during the excitation transient, which matches our expectations (see Fig. 19). The resistivity of mica tape is very high and, thus, the accumulated charges deplete slowly along the mica surfaces. The external discharges occur on the metal terminals and then

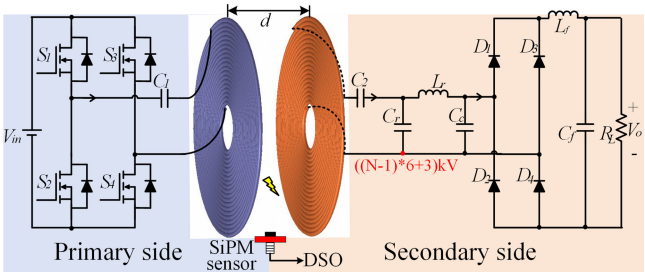

Fig. 20. Surface discharge monitoring for coils of WPT used in the auxiliary power supply circuit with an adjustable gap.

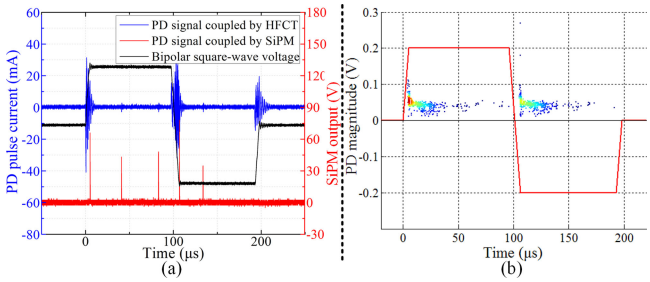

Fig. 21. Experimental results of the point discharge from the WPT coils by using the SiPM-based sensor (hollow wire type). (a) PD waveform. (b) PRPD pattern.

develop along the mica surfaces, which lead to a PRPD pattern that very closely approximates the typical surface discharge pattern, as described above. Therefore, the peak-to-peak value of the bipolar square wave excitation should be considered for E-field estimation. External discharges have been demonstrated to occur on the triple junction of metal-mica-air interfaces.

After applying the high permittivity stress control layer along the terminations, surface discharges are not captured by the SiPM sensor until the bipolar excitation reaches a peak value of approximately 6 kV. This improvement in PDIV matches our simulation results (see Fig. 18). We also test this design in the H-bridge circuit equipped with 10-kV SiC MOSFET modules. Under 10-kHz bipolar excitation (positive and negative are 50% duty cycle, *dV/dt* is around 50 V/ns, and deadtime is 1 μs), its PDIV is reduced to approximately 5.2 kV_{pk}. Therefore, the experimental assessment with the worst operating conditions demonstrates that the design requirement is satisfied with the improved version.

B. External Insulation Design and Assessment of WPT Circuit via SiPM PD Detection Sensor

For the WPT circuit used in the auxiliary power supply system, the primary side reference voltage of the WPT circuit is the real ground, while the secondary side reference voltage of the WPT circuit depends on the converter operation mode. In general, the entire converter system voltage should be blocked between the energy transferring and receiving coils. Because of the four PEBBs in the series, and ±12-kV dc input per arm, the air clearance between the two coils should be properly selected to isolate ±12-kV bipolar excitation.

In the experimental setup, the air gap between the two coils could be adjusted (see Fig. 20). To enable a more uniform E-field distribution and reduce the air gap distance between the two coils, hollow copper wires (with no insulating coating) are considered for constructing the two coils instead of using Litz wire [23]. If a different material, such as epoxy, is applied as the major insulation between coils, the parasitic capacitance becomes higher owing to the much higher permittivity of epoxy. A greater capacitance between the two coils impairs the EMI mitigation of this design, as it will apply a lower common mode (CM) impedance path to earth. The entire optimization procedure of the insulation distance, EMI mitigation, and circuit efficiency for this design will be discussed in a future study.

In the optimized result, only air is used between the two coils to keep the CM parasitic capacitors as small as possible. The conformal coating is considered to enhance the insulation of the hollow wires. Point discharge could be captured by the SiPM sensor under bipolar square wave excitation with a peak value of 15 kV (see Fig. 21). The distance between the two coils is 20 mm under this test. A 1.5 safety factor is applied to compensate for the possible change in air property, variation in surface roughness, and mechanical assembly tolerance.

After further increasing the insulation distance to 30 mm, the insulation is verified again, and no external discharge is captured at the maximum output of the commercial power source. Our experimental conditions are limited by the power source to include the most rigorous parameters: bipolar square wave excitation with a 25-kV peak value and a 2.5-kHz frequency, as well as a positive and negative pulse width of 100 μs with a maximum equivalent *dV/dt* of approximately 40 V/ns. Moreover, this design is tested in an H-bridge circuit equipped with 10-kV SiC MOSFET modules. Under 10-kHz bipolar excitation (positive and negative are 50% duty cycle, *dV/dt* is around 60 V/ns, and deadtime is 1 μs.) with approximately 7 kVpk, no point discharges are captured. The output voltage amplitude is limited by the H-bridge circuit and the used 10 kV module packaging.

Because we apply a relatively large safety factor based on the E-field FEA simulation, the maximum E-field intensity along the edges of the correctly fabricated coils is well controlled during normal operation voltage. Based on the tests that we already completed, we believe that this design could satisfy the practical application requirements.

VI. Conclusion

External insulation is a critical aspect in the design of converters. This study introduced a SiPM-based sensor that accurately and efficiently detects external discharge, especially under square wave excitation. Experimental results demonstrate that this compact SiPM-based sensor has very good sensitivity and pulse resolution, as well as high immunity to EMI. This novel sensor can be used for offline assessment of converters and even online insulation monitoring in the future.

Owing to use of the SiPM sensor, two representative discharge models were constructed for PD behavior characterization under square wave excitation with varied parameters. After analyzing the test data, the comprehensive physic mechanism was given

for the surface and point discharge models, respectively. These physical mechanisms could explain the similarities and differences between the two discharge models, thereby providing a deeper understanding of the test data.

A further exploration of the changes of PDIV and PD statistic parameters in relation to excitation polarity, rising/falling time, frequency, amplitude, and other factors may inform future related work, such as fast aging and reliability tests.

Based on the results of this article, some generalized suggestions for external insulation design and assessment were developed and summarized. They help indicate the worst case that should be considered for both external insulation design and assessment if the square wave excitation parameters change during real operation. Meanwhile, our suggestions provide ways to distinguish surface and point discharges during acceptance tests under square wave excitation, which helps with insulation diagnoses and localizations.

Finally, we developed a guide for the iteration process that could be used when designing and assessing the external insulation of MV converters. We demonstrated the use of this flowchart with two examples, described in Section V, to assist other engineers in their own practice if similar issues appear during the design of other converters.

REFERENCES

[1] G. Ortiz, M. G. Leibl, J. E. Huber, and J. W. Kolar, "Design and experimental testing of a resonant DC–DC converter for solid-state transformers," *IEEE Trans. Power Electron.*, vol. 32, no. 10, pp. 7534–7542, Oct. 2017.

[2] Q. Zhu, L. Wang, A. Q. Huang, K. Booth, and L. Zhang, "7.2-kV single-stage solid-state transformer based on the current-fed series resonant converter and 15-kV SiC MOSFETs," *IEEE Trans. Power Electron.*, vol. 34, no. 2, pp. 1099–1112, Feb. 2019.

[3] S. Madhusoodhanan, K. Mainali, A. K. Tripathi, A. Kadavelugu, D. Patel, and S. Bhattacharya, "Power loss analysis of medium-voltage three-phase converters using 15-kV/40-A SiC N-IGBT," *IEEE J. Emerg. Sel. Topics Power Electron.*, vol. 4, no. 3, pp. 902–917, Sep. 2016.

[4] J. Wang *et al.*, "Design and testing of 6 kV H-bridge power electronics building block based on 10 kV SiC MOSFET module," in *Proc. Int. Power Electron. Conf.*, 2018, pp. 3985–3992.

[5] A. Christe, E. Coulinge, and D. Dujic, "Insulation coordination for a modular multilevel converter prototype," in *Proc. 18th Eur. Conf. Power Electron. Appl.*, 2016, pp. 1–9.

[6] Y. Xu *et al.*, "Medium voltage sic based converter laminated bus insulation design and assessment," *IEEE J. Emerg. Sel. Topics Power Electron.*, vol. 7, no. 3, pp. 1715–1726, Sep. 2019.

[7] D. Rothmund, D. Bortis, and J. W. Kolar, "Highly compact isolated gate driver with ultrafast overcurrent protection for 10 kV SiC MOSFETs," *CPSS Trans. Power Electron. Appl.*, vol. 3, no. 4, pp. 278–291, Dec. 2018.

[8] J. Wang, S. Mocevic, Y. Xu, C. DiMarino, R. Burgos, and D. Boroyevich, "A high-speed gate driver with PCB-embedded rogowski switch-current sensor for a 10 kV, 240 A, SiC MOSFET module," in *Proc. IEEE Energy Convers. Congr. Expo.*, 2018, pp. 5489–5494.

[9] Y. Xu, M. Ghessemi, J. Wang, R. Burgos, and D. Boroyevich, "Electrical field analysis and insulation evaluation of a 6 kV H-bridge power electronics building block (PEBB) using 10 kV SiC MOSFET devices," in *Proc. IEEE Energy Convers. Congr. Expo.*, 2018, pp. 2428–2435.

[10] "Electrical insulating materials and systems—Electrical measurement of partial discharges (PD) under short rise time and repetitive voltage impulses," IEC TS 61934:2011.

[11] M. Ren *et al.*, "Fault prediction of gas-insulated system with hypersensitive optical monitoring and spectral information," *Int. J. Elect. Power Energy Syst.*, vol. 119, Jul. 2020, Art. no. 105945.

[12] G. C. Montanari, R. Hebner, P. Morshuis, and P. Seri, "An approach to insulation condition monitoring and life assessment in emerging electrical environments," *IEEE Trans. Power Del.*, vol. 34, no. 4, pp. 1357–1364, Aug. 2019.

[13] M. Ren, J. Zhou, B. Song, C. Zhang, M. Dong, and A. Ricardo, "Towards optical partial discharge detection with micro silicon photomultipliers," *Sensors*, vol. 17, no. 11, Nov. 2017, Art. no. 2595.

[14] P. Wang, Y. Li, A. Cavallini, J. Zhang, E. Xiang, and K. Wang, "The influence of relative humidity on partial discharge and endurance features under short repetitive impulsive voltages," in *Proc. IEEE Conf. Elect. Insul. Dielect. Phenomena*, 2018, pp. 506–509.

[15] W. Wang *et al.*, "The effect of temperature and humidity on corona inception voltage gradient of UHV DC transmission line," in *Proc. Int. Conf. Condition Monitoring Diagnosis*, 2008, pp. 816–818.

[16] D. Fabiani, G. C. Montanari, A. Cavallini, and G. Mazzanti, "Relation between space charge accumulation and partial discharge activity in enameled wires under PWM-like voltage waveforms," *IEEE Trans. Dielect. Elect. Insul.*, vol. 11, no. 3, pp. 393–405, Jun. 2004.

[17] A. Madonia, P. Romano, T. Hammarstrom, S. M. Gubanski, F. Viola, and A. Imburgia, "Partial discharge of gel insulated high voltage power modules subjected to unconventional voltage waveforms," in *Proc. IEEE Conf. Elect. Insul. Dielect. Phenomena*, 2016, pp. 715–718.

[18] Z. Yan and D. Zhu, *High Voltage Insulation Technology*. Beijing, China: China Electric Power Press, 2002.

[19] T. Hammarstrom, "Partial discharge characteristics at ultra-short voltage risetimes," *IEEE Trans. Dielectr. Elect. Insul.*, vol. 25, no. 6, pp. 2241–2249, Dec. 2018.

[20] A. Cavallini, E. Lindell, G.C. Montanari, and M. Tozzi, "Inception of partial discharges under repetitive square voltages: Effect of voltage waveform and repetition rate on PDIV and RPDIV," in *Proc. Annu. Rep. Conf. Elect. Insul. Dielect. Phenomena*, 2010, pp. 1–4.

[21] P. Wang, G. Wu, Y. Luo, and G. Zhu, "Effect of repetitive square voltage frequency on partial discharge feature," *Sci. China-Technolo. Sci.*, vol. 56, no. 6, pp. 1313–1321, Jun. 2013.

[22] N. L. Allen *et al.*, "Effects of humidity on corona inception in a diverging electric field," *IEE Proc.-A-Sci. Meas. Technol.*, vol. 128, no. 8, pp. 565–570, 1981.

[23] B. Wunsch, D. Zhelev, and B. Oedegard, "Externally-fed auxiliary power supply of MMC converter cells," in *Proc. 18th Eur. Conf. Power Electron. Appl.*, 2016, pp. 1–10.

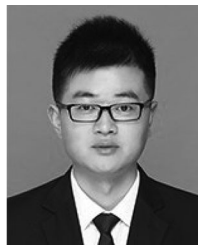

Chongxing Zhang received the B.S. degree in electrical engineering in 2003 from Xi'an Jiaotong University, Xi'an, China, where he is currently working toward the Ph.D. degree.

He is currently specializing in the smart situation awareness technology for power equipment and the insulation design and assessment for MV power electronic converters. His major research interests include high-voltage engineering and his research interests include gaseous discharge, PD detection and diagnosis, and insulation status assessment of power equipment.

Yue Xu (Student Member, IEEE) received the B.S. degree from Xi'an Jiaotong University, Xi'an, China, in 2012, and the M.S. degree from the Illinois Institute of Technology, Chicago, IL, USA, in 2015, both in electrical engineering. He is currently working toward the Ph.D. degree with the Center for Power Electronics Systems, Virginia Tech, Blacksburg, VA, USA.

His current research interests include insulation design, offline assessment and online monitoring for medium/high voltage, and high power density power electronics equipments.

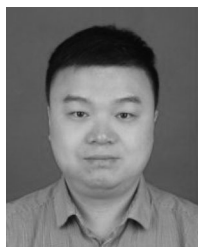

Ming Dong (Member, IEEE) was born in Shaanxi Province, China, in 1978. He received the B.S. and Ph.D. degrees in electrical engineering from Xi'an Jiaotong University, Xi'an, China, in 2001 and 2006, respectively.

In 2007, he was as a Lecturer with Xi'an Jiaotong University, where he currently works as a Professor with HV Technology Institute, School of Electrical Engineering. His major research interests include the aging mechanism of dielectric material and his research interests include intelligent HV equipment and power condition assessment.

Rolando Burgos (Member, IEEE) received the B.S. degree in electronics engineering, the Electronics Engineering Professional degree, and the M.S. and Ph.D. degrees in electrical engineering from the University of Concepción, Concepción, Chile, in 1995, 1997, 1999, and 2002, respectively.

In 2002, he joined the Center for Power Electronics Systems, Virginia Polytechnic Institute and State University (Virginia Tech), Blacksburg, VA, USA, where he was a Postdoctoral Fellow, a Research Scientist, and a Research Assistant Professor. In 2009, he joined ABB Corporate Research, Raleigh, NC, USA, where he was a Scientist and a Principal Scientist. In 2010, he was an Adjunct Associate Professor with the Department of Electrical and Computer Engineering, North Carolina State University, Raleigh, NC, USA. In 2012, he returned to Virginia Tech, where he is currently a Professor with The Bradley Department of Electrical and Computer Engineering, CPES, where he has been Professor and Member of the CPES Executive Board since 2019. His research interests include high power density wide-bandgap semiconductor-based power conversion low voltage and medium voltage applications, packaging and integration, electromagnetic interference and electromagnetic compatibility, multiphase multilevel power converters, modeling and control, grid power electronics systems, and the stability of ac and dc power systems.

Dr. Burgos is a member of the IEEE Power Electronics Society, where he currently serves as the Chair of the Technical Committee on Power and Control Core Technologies.

Ming Ren (Member, IEEE) was born in Shaanxi Province, China, in 1987. He received the B.S. and Ph.D. degrees in electrical engineering from Xi'an Jiaotong University, Xi'an, China, in 2009 and 2013, respectively.

In May 2014, he was a Lecturer with Xi'an Jiaotong University, where he is currently an Associate Professor with HV Technology Institute, School of Electrical Engineering. His major research interests include high voltage engineering and his present research interests include are risk assessment of UHV/EHV power equipment, insulation status diagnosis, and advanced fault detection and protection technologies for power systems.

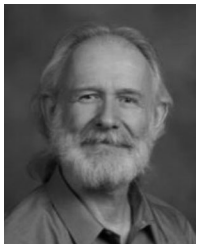

Dushan Boroyevich (Fellow, IEEE) received the Dipl.-Ing. degree from the University of Belgrade, Belgrade, Serbia, in 1976, the M.S. degree from the University of Novi Sad, Novi Sad, Serbia, in 1982, (previously Yugoslavia), and the Ph.D. degree from the Virginia Polytechnic Institute and State University (Virginia Tech), Blacksburg, VA, USA, in 1986.

From 1986 to 1990, he was an Assistant Professor and the Director of the Power and Industrial Electronics Research Program with the Institute for Power and Electronic Engineering, University of Novi Sad. In 1990, he joined The Bradley Department of Electrical and Computer Engineering, Virginia Tech, as an Associate Professor. He is currently the University Distinguished Professor with the Department and Director of the Center for Power Electronics Systems (CPES), Virginia Tech. His current research interests include electronic energy systems, multiphase power conversion, power electronics systems modeling and control, and integrated design of power converters.

Dr. Boroyevich is a member of the U.S. National Academy of Engineering. He was the recipient of the numerous awards, including the IEEE William E. Newell Power Electronics Technical Field Award and the European Power Electronics Association Outstanding Achievement Award. From 2011 to 2012, he was the President of the IEEE Power Electronics Society.